Research Article | Vol. 11, No. 9 / 1 Sep 2021 / Optical Materials Express 3111
Optical Materials EXPRESS

Free-standing tantalum pentoxide waveguides for gas sensing in the mid-infrared

MAREK VLK,[1,4] ANURUP DATTA,[1] SEBASTIÁN ALBERTI,[1] GANAPATHY SENTHIL MURUGAN,[2] ASTRID AKSNES,[3,1] AND JANA JÁGERSKÁ[1,3,5]

[1]Department of Physics and Technology, UiT The Arctic University of Norway, NO-9037 Tromsø, Norway
[2]Optoelectronics Research Centre, University of Southampton, Southampton, SO17 1BJ, UK
[3]Department of Electronic Systems, Norwegian University of Science and Technology, 7491 Trondheim, Norway
[4]marek.vlk@uit.no
[5]jana.jagerska@uit.no

Abstract: Typical applications of integrated photonics in the mid-infrared (MIR) are different from near-infrared (telecom) range and, in many instances, they involve chemical sensing through MIR spectroscopy. Such applications necessitate tailored designs of optical waveguides. Both cross-sectional designs and processing methods of MIR waveguides have been a subject of extensive research, where material transparency and substrate leakage of guided modes have been the most common challenges. Both these challenges can be solved simultaneously with air-suspended waveguides. In this paper, tantalum pentoxide (Ta_2O_5, tantala) thin films deposited on silicon were tested for two different dry under-etching procedures, XeF_2 and SF_6 plasma, with both of them facilitating selective removal of silicon. We analyze the advantages and limitations of these two methods and optimize the processing for fabricating membranes with arbitrary length and cross-sectional aspect ratio over 300. The performance of these high-aspect-ratio membranes as a framework for single-mode waveguides is rigorously analyzed at 2566 nm wavelength. With tantala being transparent up to 10 μm wavelength, such waveguides are particularly well suited for gas sensing in MIR.

1. Introduction

Integrated mid-infrared (MIR) photonics holds promise for new applications outside of telecom such as chemical and biological sensing [1]. However, as a young area of study, it presents researchers with several challenges in the development of both active and passive components. Material transparency, being the major challenge, is limited by the onset of phonon absorption at longer wavelengths, requiring careful material selection. Optical materials have been recently reviewed showing multiple candidates for adoption in MIR such as chalcogenide glasses, semiconductors, or metal oxides [2–4]. However, besides the intrinsic absorption mechanisms, materials may often contain residuals which cause additional propagation loss. Particularly in amorphous materials, the most detrimental residuals are water [5–7] and hydroxyl groups in oxides [8], as well as N–H bonds in nitrides [9–11]. Fortunately, their content can be reduced by improving material packing density and by annealing. Material challenges in optical waveguides, mainly absorption, can also be solved by careful design. Optical waveguides can be engineered to minimize light confinement in a lossy material. It has been reported that the silicon-on-insulator (SOI) platform can be used beyond the silica transparency edge at ~3.6 μm with strong light confinement in a relatively thick silicon waveguide core [12]. Nevertheless, if the optical mode is

#430994 https://doi.org/10.1364/OME.430994
Journal © 2021 Received 11 May 2021; revised 29 Jun 2021; accepted 9 Jul 2021; published 23 Aug 2021

Optical Materials EXPRESS

nearly entirely confined in the solid core, the interaction with the surrounding environment is minimal and such waveguides are then ill-suited for applications in sensing.

Another common obstacle at longer wavelengths is substrate leakage. Commercially available wafers, originally intended for telecom applications, exhibit bottom claddings too thin relative to the wavelength and light distribution in the MIR and fail to isolate the guided mode from the substrate. Suspending the waveguide in air can directly avoid this issue. Such an architecture allows for a maximum refractive index contrast, keeping the light further away from the substrate. In this context, much attention has been given to the SOI material platform, where silicon waveguides have been suspended via selective removal of SiO_2 by HF etching [13–16]. Free-standing germanium waveguides have been made in a similar way from either germanium-on-insulator (GOI) [17] or Ge-on-SOI [18]. In an alternative approach, silicon has been removed directly from below the device layer, allowing the air cladding to be extended as much as needed in contrast to the limited oxide thickness. Diamond waveguides have been under-etched in SF_6 plasma [19] while dry etch with XeF_2 has been used to release SiO_2 microdisks [20] and silicon waveguides on thin oxide membrane [21] for operation in the near-infrared (NIR) domain. Moreover, the MIR transparency range of silicon has been fully exploited by wafer bonding [22]: The air cladding has been first defined as trenches in a silicon wafer and a silicon device layer has been bonded over the wafer. Waveguides have been finally patterned onto the membranes, which resulted in an all-silicon structure. However, the full protocol is rather complex.

In addition, membrane waveguides with extended evanescent field can be tailored for a variety of other applications such as chip-based microscopy where the evanescent field is used to excite biological samples on the waveguide surface at visible wavelengths [23,24]. Here, penetration depths of 100–200 nm provide an ideal optical cross-section for high contrast images. Thin membranes are also found in various MEMS devices like thermal [25], and pressure sensors [26], or optical filters [27], and similar membrane processing has been used for wafer-scale preparation of transmission electron microscope specimens [28] and for constructing cages for DNA trapping [29].

In this paper, we report on processing tantalum pentoxide (Ta_2O_5, tantala) into air-suspended waveguides to tackle the challenges of core material absorption and substrate leakage. The potential of tantala in integrated optics has been manifested by low-loss optical waveguides of 0.78 dB cm^{-1} at 660 nm [30], and 0.65 dB cm^{-1} at 1600 nm [31]. Its intrinsic transparency ranges approximately from 0.5 to 10 µm [32], rendering tantala suitable for MIR nanophotonics. We chose a design of a free-standing membrane with a rib waveguide [13,17–19,22,33] and optimized its dimensions for spectroscopic detection with TM-polarized light in the MIR. The optical field is strongly delocalized, which has the following consequences: The light–matter interaction in air is unprecedently strong and the field extends far from the waveguide core, requiring large air buffer between the waveguide and the substrate. In the present approach, the device layer rests directly on top of a silicon wafer which is then selectively, locally removed from below the waveguides and results in thick air cladding, which isolates the guided light from the substrate. For the purpose of the under-etching, we compare spontaneous etching with XeF_2 gas and plasma etching with SF_6 in terms of material selectivity, suitable masking materials, etch profile, and ease of processing.

2. Design

Air-suspended waveguides can effectively remove substrate leakage and, if sufficiently thin, they can increase the overlap of the guided light with the surrounding air cladding. Our waveguide (Fig. 1) is formed by a shallow rib in the tantala membrane. It was modeled with finite-difference eigenmode solver MODE (Lumerical) to determine appropriate dimensions for the TM-polarized light at 2566 nm. We identified four figures of merit that depend on the dimensions and thus allow finding the optimal design in terms of light–analyte interaction and propagation loss. First,

Optical Materials EXPRESS

it is the external confinement factor Γ_{ext} [33–37], which quantifies the interaction strength outside the waveguide core, accounting for light field distribution and dispersion. It depends mainly on the membrane thickness T and remains unaffected by the rib width W or etch depth E. Second, the lateral leakage, characteristic for TM modes in rib waveguides [38], shows minima dependent on the rib width W while the magnitude is driven by the etch depth E. Third, bending loss is a function of all dimensional parameters but mainly E. Fourth, and last, the waveguide needs to support a single mode at the selected polarization. While Γ_{ext} is nearly the same for different TM modes in multimode devices, propagation loss due to the lateral leakage and bends varies. Intermodal interaction leads to increased noise, and in some cases completely hinders a correct interpretation of the transmission signal.

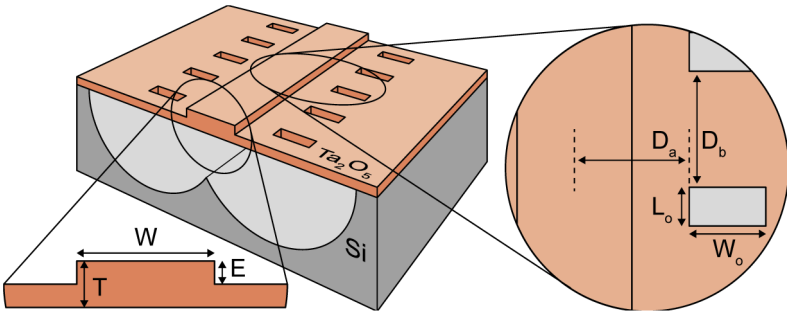

Fig. 1. Schematics of the air-suspended tantala waveguide. The cross-sectional parameters include the as-deposited layer thickness T, rib width W, and etch depth E. The top view shows etching openings, which facilitate the under-etching. $W_o \times L_o$ are the openings dimensions and D_a and D_b are the lateral and longitudinal spacings.

For tantala as the waveguide core material, Γ_{ext} reaches maximum of 109% around 400 nm device layer thickness T for the wavelength of 2566 nm (Fig. 2(a)). Figure 2(b) indicates the positions of lateral loss minima for T = 400 nm and etch depth E = 50 nm. Figure 2(c) shows the single-mode condition in the E–W parameter space where only a single mode is supported anywhere below the curve. Based on these calculations, we targeted the loss minimum around 4.7 μm rib width with 50 nm etch depth close to the single-mode threshold in order to maintain the bending loss below 0.1 dB per 90° for 1 mm radius of curvature. A higher etch depth decreases the bending loss further but also increases the maximum lateral leakage [39]. The model for T = 400 nm, E = 50 nm, and W = 4.7 μm also predicts a uniquely low end-fire in-coupling loss (Fig. 2(d)) with a minimum of 0.65 dB for a 4.2 μm beam diameter.

The under-etching is done from the front side and therefore necessitates etching openings through the device layer. The openings must be positioned sufficiently far from the waveguide not to disturb the guided mode. We approximated the effect by placing perfectly matched layers (absorbing boundary conditions) on the sides of the simulation domain and varied the domain width. The effect should be negligible already around D_a = 20 μm. The dimensions of the etching openings were determined experimentally as discussed later.

Optical Materials EXPRESS

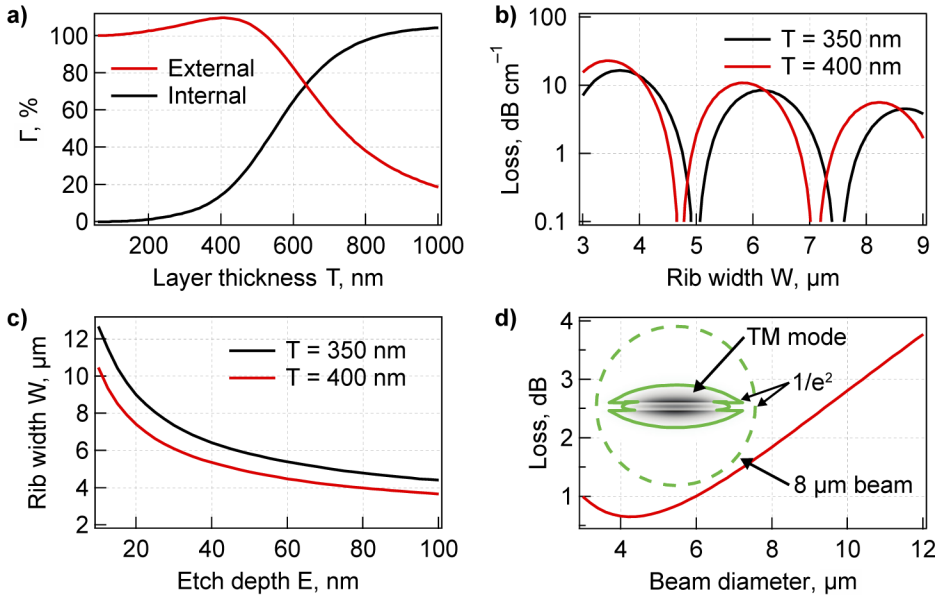

Fig. 2. Waveguide model results for TM polarization and at 2566 nm wavelength for E = 50 nm, and $n_{Ta2O5} = 2.1$. Layer thickness and rib width are T = 400 nm and W = 4.7 µm if not stated otherwise. **a)** Confinement factor Γ in air (external, Γ_{ext}) and in the core material (internal, Γ_{int}) as a function of layer thickness T. **b)** Propagation loss due to lateral leakage of the rib waveguide guided TM mode. **c)** Single-mode condition in the E–W parameter space. **d)** In-coupling loss between a free-space beam and the fundamental TM mode. Inset illustrates the overlap between the TM mode power (P_z) distribution and Gaussian beam focus of 8 µm diameter. The green contours indicate $1/e^2$ power levels for the mode (solid), and the beam (dashed).

3. Processing

Tantala thin films can be prepared by various methods [40] such as physical vapor deposition (PVD) [6,7,31,41–43], chemical vapor deposition (CVD) [44], or from a solution [30,32,45]. It features a high refractive index around 2.1 at 1550 nm and 2.05 at 2500 nm, and the broad transparency (0.5–10 µm) as discussed in the introduction. However, this transparency window is often obscured by wide water and OH absorption bands, one being centered at 3 µm [6–8,32].

The process flow for fabricating the suspended waveguides is illustrated in Fig. 3. It begins with deposition of the tantala device layer (step 1) onto a standard <100> Si wafer. We prepared 3 samples in this study as listed in Table 1 with the tantala films deposited by RF magnetron sputtering (A1, in-house), plasma-assisted e-beam evaporation (A2, purchased from Helia Photonics), and sol-gel (A3, in-house).

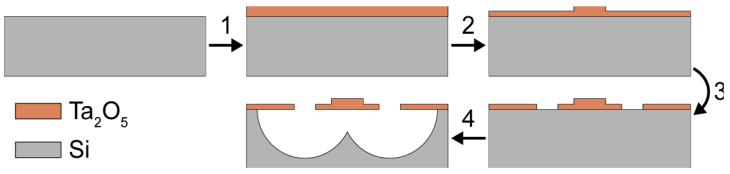

Fig. 3. Process flow for fabrication of suspended waveguides. Film deposition (1) is followed by consecutive patterning of waveguides (2) and etching openings (3). In the final step, the waveguide is under-etched (4).

Optical Materials EXPRESS

Table 1. Summary of processing methods and target dimensions for samples A1–A3.

Sample	Deposition method	Target layer thickness T	Shallow etching	Target dimensions		Under-etching method
				Rib width W	Etch depth E	
A1	Magnetron sputtering	350 nm	Ar IBM	4.5 μm	30 nm	XeF_2 gas
A2	E-beam evaporation	400 nm	CHF_3/O_2 ICP-RIE	4.9, 5.3, 5.7 μm	50 nm	SF_6 plasma
A3	Sol-gel	400 nm	CHF_3/O_2 ICP-RIE	—	—	SF_6 plasma

Following the deposition, the patterning was performed in two steps to accommodate for the difference in the etch depths of the ribs and the etching openings: The ribs are relatively shallow, up to 50 nanometers, while the etching openings need to penetrate the whole device layer(s). Table 1 lists the target values of E and W. Sample A1 was patterned with a positive tone photoresist and UV photolithography (Süss MA-6, $\lambda = 385$ nm) in hard contact mode followed by Argon ion beam milling (IBM, Oxford Instruments Ionfab 300+). Further details on the fabrication of sample A1 have been reported in [33]. For the processing of samples A2 and A3, we used mask-less lithography (Heidelberg Instruments MLA150, $\lambda = 405$ nm) followed by pattern transfer with inductively coupled plasma reactive ion etching (ICP–RIE, Plasmalab System 100 ICP–RIE 180). Plasma chemistries of CF_4 [30], C_4F_8/O_2 [42], CHF_3/Ar [45] have been reported for tantala etching and we optimized CHF_3/O_2 chemistry with flow rates 48/2 sccm, 20 mTorr pressure, 100 W RF and 1000 W ICP powers.

3.1. Under-etching

Two different methods of under-etching, namely XeF_2 molecular gas etching and inductively coupled plasma with SF_6, were tested and compared. Both gases primarily serve as sources of fluorine, which is highly reactive and forms volatile compounds with Si and many transition metals. Notably, XeF_2 etches Si spontaneously while SF_6 needs an external supply of energy to release fluorine radicals and ions. The etch rates with respect to the under-cut depth are functions of pressure [46–49] and aperture size [48–50] and they are nonlinear in time with respect to the under-cut depth [50].

XeF_2 dry etching was applied for under-etching of sample A1. The compound has been studied since the late 1970s for Si etching [51] and the reaction equation reads [46,52]

$$2XeF_2 + Si \rightarrow 2Xe + SiF_4. \tag{1}$$

Si is etched rapidly and selectively over some materials like SiO_2, Si_3N_4, Al_2O_3, or photoresists [51,53,54], rendering them suitable as mask materials. To the best of our knowledge, XeF_2–Ta_2O_5 interaction has not been studied before and therefore we tested the selectivity between the two materials. The instrument (Xactix) was operated in a pulsed mode with alternating etch steps, with XeF_2/N_2 mixture, and purge steps with N_2. Both materials were exposed from the top and we varied the XeF_2:N_2 ratio and etch pulse duration in the experiment. Total pressure and delay between the pulses were kept constant.

Samples A2 and A3 were under-etched in SF_6 plasma in ICP–RIE. Unlike the XeF_2 etcher, the ICP–RIE system operates continuously and SF_6 flow rate, process pressure, and RF and ICP powers are all variable, and can be tuned for optimum etch rate. For isotropic etching, RF source is not used (0 W power). The reactions between liberated fluorine and silicon lead again to the formation of SiF_4, but fluorine is released in the plasma by several dissociation steps

$$\begin{aligned} e + SF_x &\rightarrow SF_{x-1}^- + F \\ &\rightarrow SF_{x-1} + F^- \\ &\rightarrow SF_{x-1} + F + e \end{aligned} \tag{2}$$

where x = 4–6 [55]. The selectivity towards other materials is similar to that of XeF_2.

Optical Materials EXPRESS

Top passivation of tantala was mandatory in both processing methods because tantala does not withstand direct exposure to the etchants. Bottom passivation was also studied by depositing thin layers of more resistant dielectrics below tantala by the same respective methods (see Table 1). Requirements for the bottom passivation were found to differ for both methods. Besides passivation, optimization of the processes was done in terms of the total etching duration, etching openings dimensions ($W_o \times L_o$), and pressures.

4. Results

Under-etching of tantala was conducted successfully with both XeF_2 in sample A1 and SF_6 plasma in sample A2. Nevertheless, notable differences were observed in the processing methods and they are discussed in the following sections in detail. After the processing was optimized, we patterned the tantala films with rib waveguides in the final fabrication rounds.

4.1. XeF_2

The Si:Ta_2O_5 selectivity was found toF 210 ± 40 with no clear dependence on the XeF_2:N_2 ratio or etch step duration. The large deviation is attributed to a low homogeneity of the etch rate over the etching chamber area. In addition, Fig. 4(a) demonstrates that tantala is removed rapidly also during under-etching. It is therefore unlikely that the recipe can be optimized for sufficient selectivity, and bottom passivation is required to make membranes with aspect ratio of 300 and more as required for the selected waveguide design. Figure 4(b) shows a result with a 10 nm thick SiO_2 passivation layer inserted between silicon and tantala, which was then protected over a lateral distance of a few micrometers. Although the etch rate ratio of silicon to SiO_2 is reportedly high, ranging from less than 1000 [52] up to near infinity [51,53,56,57], it did not prove sufficient in our processing scenario. Possible causes are the quality of the oxide [58], and etching Si in proximity of SiO_2 because the XeF_2–Si reaction facilitates the release of fluorine radicals, which further attack SiO_2 [59]. Moreover, exposure through small openings has been shown to deteriorate the selectivity [52]. On the other hand, passivation with 30 nm aluminum oxide (Al_2O_3, alumina) on top of a 30 nm buffer SiO_2 layer for improved adhesion between alumina and silicon showed excellent performance with no observed degradation of the alumina film as captured in Fig. 4(c).

The progression of the under-etching strongly depends on the dimensions of the openings. Early experiments showed that openings of 3×3 µm^2 (Fig. 4(a),(b)) with D_a being either 34 or 24 µm and $D_b = 7$ µm significantly limited the etch rate. The openings were therefore enlarged to 10×5 µm^2 (Fig. 4(c)) and the spacings adjusted to $D_a = 24$ µm and $D_b = 25$ µm to enable complete under-etching. Final process conditions were set to 270 cycles of 5 s etch pulses with XeF_2/N_2 pressures of 3/2 Torr and 10 s purging with N_2. The resulting profile of the under-etching appears perfectly isotropic as seen in the cross section in Fig. 5(a), and the membrane appears homogenous in a top view as seen with an optical microscope in Fig. 6(a).

4.2. SF_6

The most critical parameter in the SF_6 plasma isotropic etching through small openings is the process pressure, and 50 mTorr maintained a sufficient etch rate. Figure 7 shows samples of an under-etching progression with varying longitudinal spacing D_b and openings dimensions $W_o \times L_o$ after 30 min with 100 sccm SF_6, 50 mTorr, 1500 W ICP power. The lateral spacing $D_a = 30$ µm was fixed and followed from the numerical model. The etch rates are limited by diffusion within the studied range of openings dimensions [49]. Based on this empirical test, we chose 15×7.5 µm^2 openings and $D_b = 40$ µm and extended the etching time to 60 min. The final recipe was 50 mTorr, 100 sccm SF_6 flow, 1500 W and 0 W of ICP and RF power respectively. The substrate can heat up during the process and cause the photoresist used as a mask to burn. It is therefore imperative to perform the etching in shorter sequences to let the substrate cool down.

Optical Materials EXPRESS

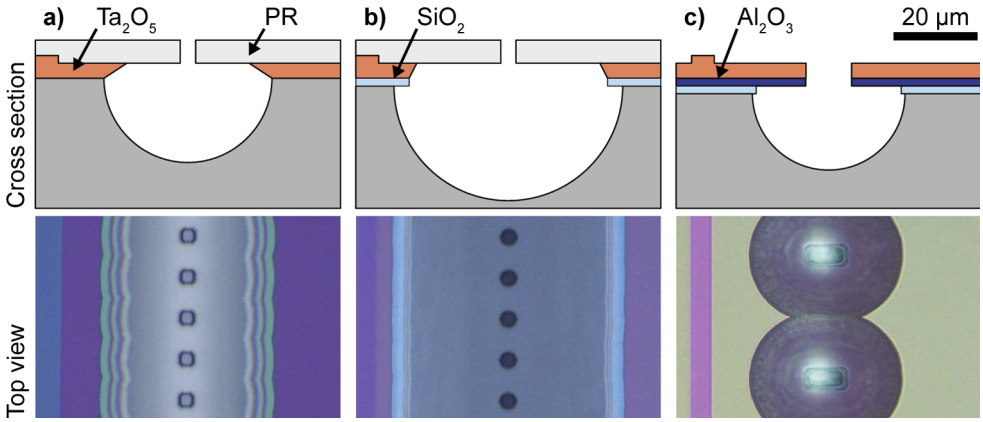

Fig. 4. Gradual inclusion of passivation layer in XeF_2 under-etching of Ta_2O_5. The etching in these images was not completed and only a single row of etching openings is displayed. Cross section provides schematics corresponding to the top view images acquired with an optical microscope. **a)** The sample was etched with no bottom passivation while the top was protected by a photoresist (PR). **b)** 10 nm SiO_2 passivation was used in the bottom. **c)** 30 nm Al_2O_3 passivation and 30 nm SiO_2 adhesion layers were used to aid the processing. The top photoresist was removed.

In this study, 5 min periods of etching were interlaced with 3 min plasma-less N_2 flow (50 sccm, 40 mTorr).

This recipe was applied for processing of samples A2 and A3. Sample A2, which featured SiO_2 adhesion layer and Al_2O_3 passivation layer, was successfully under-etched as shown in Figs. 5(b) and 6(b). Sample A3, prepared with no backside passivation, also resisted the SF_6 plasma. However, high film stress resulted in cracking of the membrane and therefore the process was interrupted already after 10 min (Fig. 6(c)).

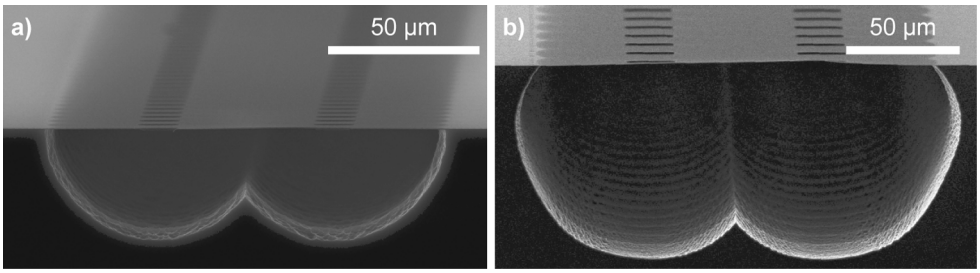

Fig. 5. Etch profiles: device layers under-etched in **a)** XeF_2 and **b)** SF_6 plasma.

After completing the under-etching of sample A2, we observed residues on the membrane backside. These are likely leftovers of the etched materials, which were passivated against the etching by photoresist contamination in the plasma [48,60]. Stylus profiler (KLA Tencor, 2 µm diameter stylus) measurement revealed that they are about 400 nm high, and energy-dispersive X-ray spectroscopy (EDS) showed a high silicon content. It was possible to remove them with a low concentration (~1%) tetramethyl ammonium hydroxide (TMAH) solution [19]. The TMAH also removed the passivation layers of SiO_2 and Al_2O_3, leaving a single-layer free-standing Ta_2O_5 membrane shown in Fig. 7(b).

Optical Materials EXPRESS

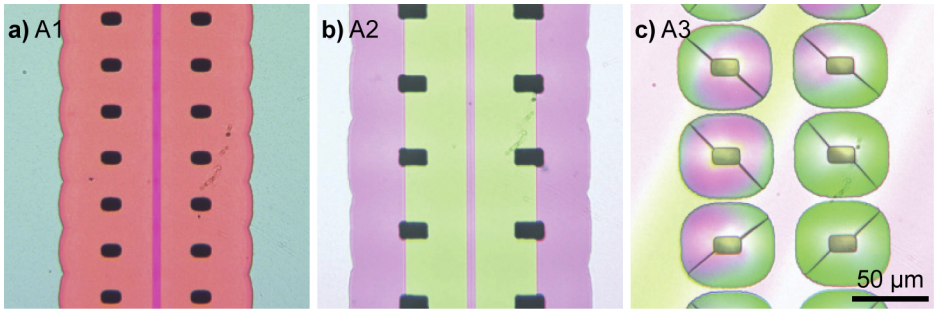

Fig. 6. Optical microscope images of the fabricated membranes. **a)** Sample A1 under-etched in XeF_2 with SiO_2 and Al_2O_3 layer stack for passivation. **b)** Sample A2 under-etched in SF_6 plasma after the TMAH treatment, which removed the SiO_2/Al_2O_3 layer stack. The shallow etching, which defines the waveguides, only extends to the openings. **c)** Sample A3 also under-etched in SF_6 plasma. The scale bar in **(c)** applies to all images.

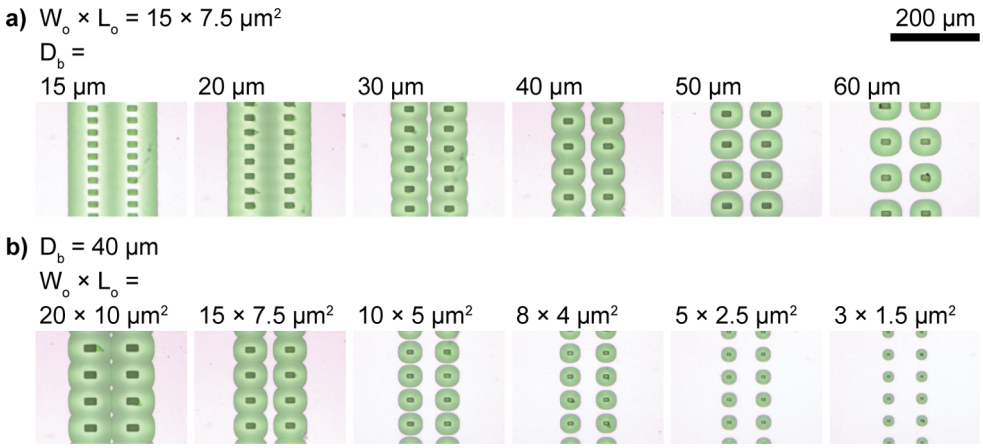

Fig. 7. Result of under-etching test in SF_6 plasma after 30 min with lateral spacing $2 \times D_a = 60\,\mu m$ between openings. **a)** Effect of different longitudinal spacings of the etching openings with dimensions $15 \times 7.5\ \mu m^2$ ($W_o \times L_o$). **b)** Effect of different openings sizes with a constant longitudinal spacing $D_b = 40\,\mu m$.

Optical Materials EXPRESS

4.3. Comparison of the etching methods

Although both isotropic methods rely on producing volatile SiF_4, there are significant differences. First, the two methods result in different profiles. XeF_2 gave highly isotropic, hemispherical etch profiles as seen in Fig. 6(a). Reactive species are allowed to distribute homogeneously within the forming cavity because the process is dominated by physisorption and dissociation at room temperature [53]. Meanwhile, SF_6 plasma exhibited a lower degree of isotropicity. Such quasi-isotropic profile (Fig. 6(b)) has also been reported elsewhere [48]. It is likely a result of the etching being dominated by direct impact of fluorine radicals [50], where any site not in the line of sight of the radical is etched slower. This effect, named neutral shadowing [61], has a visible impact on etching through small openings.

The passivation requirements in the two methods were also found to differ. Both methods were tested with and without bottom passivation and gave different under-etching selectivities, and the complete stack of layers used in the processing in all samples is listed in Table 2. This can be explained by the same mechanisms responsible for the dissimilar etch profiles. In XeF_2, tantala cannot be under-etched directly and a bottom passivation with a more resistant material, ideally Al_2O_3, is necessary (Fig. 4). XeF_2 molecules have enough time to diffuse to the tantala backside surface because silicon etching is limited by a physisorbed layer. In contrast, SF_6 plasma facilitates direct under-etching of tantala as evidenced by sample A3. Most of reactive species entering through an opening are immediately spent on the silicon etching and do not reach the device layer. Tantala is still slowly etched from the backside but this effect is not significant and does not impair the fabrication for the required membrane aspect ratio. Al_2O_3 passivation can be again used if the tantala over-etching is not affordable.

Table 2. Summary of the deposited layers and waveguide patterning on samples A1–A3.

Sample	Ta_2O_5 device layer thickness T	Al_2O_3 passivation layer thickness	SiO_2 adhesion layer thickness	Patterned waveguides
A1	350 nm	30 nm	30 nm	Yes
A2	400 nm	20 nm	20 nm	Yes
A3	400 nm	—	—	No

The top side of the device layer can be passivated with a photoresist in XeF_2 processing. In SF_6 plasma, the photoresist is etched, as discussed above, and it can burn due to accumulated heat. Either way can lead to exposing the device layer, which is highly detrimental. In addition, it has been hypothesized that the photoresist contaminates the plasma and the etched surfaces [48]. These issues could be circumvented by using a metal mask, which can be removed by liquid processing.

4.4. Mechanical stability of thin-film membranes

Thin films can develop compressive or tensile stress with respect to the substrate. If the stress magnitude is critical, bending or cracking of the membranes will occur. Deposition processes of samples A1 and A2 produced low-stress films, and their mechanical stability was further tested with a stylus profiler. The membranes were laterally scanned with the stylus with loads of 0.5, 1, and 2 mg without getting damaged. This shows that the mechanical stability is satisfactory for membranes with aspect ratio over 300. Contrarily, sample A3 could not be under-etched because cracks started developing in the layer soon after the processing initiated (Fig. 6(c)). This was likely caused by a high tensile stress in the layer, which is a consequence of the deposition from a solution.

Optical Materials EXPRESS

4.5. Waveguide patterning

Profilometer measurements revealed that the rib shallow etch depth E was about 32 nm in sample A1, close to the targeted 30 nm. The Argon IBM results in partial redeposition of the material [62,63]. The deposits are visible on edges of the waveguides in the profilometer scan in Fig. 8. This can cause local inhomogeneities and thus contribute to propagation loss by scattering. The processing method was therefore changed to RIE in sample A2 where the etched material is chemically transformed into volatile compounds and discharged from the reactor. The shallow reactive etching with CHF_3/O_2 on sample A2 gave approximately 45–50 nm, again matching well to the intended 50 nm etch depth E. In this case, material redeposition was significantly suppressed (Fig. 8).

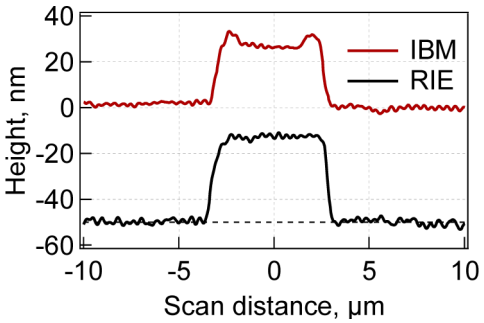

Fig. 8. Stylus profiler scans of waveguides samples A1 (red curve) and A2 (black curve). A1 was patterned via Ar IBM and shows residues of redeposition on the waveguide edges. A2 was patterned via RIE and no redeposition was observed. Note that the height of the rib produced by RIE appears to be 40 nm due to membrane bending. Measurements at different sites revealed a true height of 45–50 nm. See **Data File 1** and **Data File 2** for underlying data.

5. Application: suspended nanophotonic waveguides

As discussed in detail in the Design section, the principal benefit of the fabricated suspended rib waveguides is their ability to accommodate a strongly vertically delocalized field. In this context, operating the waveguides in TM polarization is beneficial despite the limits of lateral leakage, facilitating remarkably high Γ_{ext} [37] and thus strong light–matter interaction (Fig. 2(a)). Previously, we experimentally confirmed the high confinement factor of $107 \pm 2\%$ in sample A1 [33]. Note that both A1 and A2 designs lead to a similar external confinement factor, while A1 exhibits less interaction with the core material (and, hence, potentially lower propagation loss due to absorption) at the cost of possibly lower mechanical stability.

The waveguide pathlength L represents another mean of controlling the interaction with analyte as can be understood from a generalized Lambert–Beer law

$$I = I_0 \exp[-\alpha \Gamma L] \tag{3}$$

with α being the bulk absorption coefficient. The possible pathlength that can be achieved is principally limited by the propagation loss. This in turn comes from intrinsic material absorption, impurity and residual absorption, scattering, and lateral leakage.

Propagation loss of waveguides on sample A1 was determined from the decay of out-of-plane light scattering as well as the cutback method. We retrieved loss of 6.8 dB cm^{-1} at 2566 nm. This figure was achieved after annealing the sample at 600 °C for 3 h. Without annealing, the loss was approximately 12 dB cm^{-1}. We therefore attribute the relatively high loss to residual water

Optical Materials EXPRESS

and OH absorption because 2566 nm wavelength coincides with a wing of the water absorption band at 3 µm [5]. Annealing is expected to remove water and improve condensation reactions of adjacent O–H groups [8].

Waveguides in sample A2 did not visibly scatter light and therefore the loss was measured via the cutback method with three different waveguide lengths. The lowest loss of 9.5 dB cm^{-1} was achieved with 5.1 µm wide waveguides (see Table 3). The loss increases for both narrower and wider waveguides (4.6 and 5.5 µm wide respectively) within sample A2, which is consistent with the lateral leakage (Fig. 2(b)). No annealing was performed with sample A2 and the relatively high loss can be a result of both absence of the annealing step and stronger light confinement in the core material. Nevertheless, the evaporated layers are expected to have a higher packing density than the sputtered layers, thus leaving less space for water. Lower losses are expected after annealing, which needs to be performed prior to membrane processing in order not to damage the membranes.

Table 3. Waveguide dimensions and loss measurement at 2566 nm. The dimensions were measured with a scanning electron microscope (Zeiss Zigma). See Data File 3 and Data File 4 for loss measurement underlying data.

Sample	Width [µm]		Loss		Reference
	Nominal	Measured	Propagation [dB cm^{-1}]	Coupling [dB]	
A1	4.5	4.8	6.8	2.3	Our group in [33]
A2	4.9	4.6	12.1	2.3	This work
A2	5.3	5.1	9.5	2.7	This work
A2	5.7	5.5	14.1	–	This work

The TM mode of the fabricated waveguides has several characteristics that remind of a free space beam. The field is strongly delocalized (see inset of Fig. 2(d)), leading to a low effective index of approximately 1.1 for a 400 nm device layer. Consequently, both the facet reflections and the coupling losses in an end-fire configuration are remarkably low. With our characterization setup and the coupling objective lens with NA = 0.56, we get the minimum coupling spot of 8–10 µm in diameter, which corresponds to a theoretical 1.8–2.8 dB in-coupling loss for a 4.7 µm wide waveguide (Fig. 2(d)). The influence of the rib width W between 4.9 and 5.7 µm on the coupling loss is negligible. The experimental coupling loss per facet values for the samples A1 and A2 are between 2.3 and 2.7 dB, which is in a good agreement with the theory.

6. Conclusion

We demonstrated two dry-etch methods for the under-etching of tantala membranes for the purpose of fabricating air-suspended optical waveguides. There are significant differences in the etching results. With an Si to Ta_2O_5 selectivity of 210 ± 40, XeF_2 does not allow direct processing of tantala and a bottom passivation layer with more resistant material (Al_2O_3) is necessary as demonstrated in Fig. 4. In contrast, SF_6 plasma facilitates direct under-etching of tantala with no need for passivation (Fig. 6(c)). However, the different selectivities during the under-etching result from etch rate limiting mechanisms rather than from difference in actual material selectivities: Reactive species are depleted faster in SF_6 plasma than in XeF_2, and probabilities to reach the tantala layer backside are therefore different. Photoresist was found to be a convenient top side passivation against XeF_2 but not against SF_6 plasma. This is due to photoresist etching in the plasma and residues on the membrane backside, which were linked to fluorocarbon contamination. A hard mask, such as chromium, would be more suitable. The relaxed requirements on the backside passivation in SF_6 plasma makes the process appealing for use on other dielectrics such as TiO_2, or Si_3N_4, while Al_2O_3 can be processed either way. The resulting etch profiles (Fig. 5) favor SF_6 plasma processing, which leads to more pronounced

Optical Materials EXPRESS

separation between the device layer and the substrate. This is beneficial to preventing the delocalized guided light from leaking into the substrate.

Stylus profiler loading and wet processing of the membranes further demonstrated that fabricated membranes with an aspect ratio of up to 400 are mechanically stable. However, thin films with high tensile stress such as films deposited from wet solutions cannot be directly processed into membranes because they start cracking in an early phase of the under-etching process (Fig. 6(c)). The films thus need to be prepared low-stress, while annealing can potentially alleviate compressive stress [43].

We further demonstrated that the processed membranes can be successfully utilized as a backbone for air-suspended rib waveguides. This waveguide design is very attractive for optical sensing applications, especially in the MIR molecular fingerprint region. Waveguiding was studied at 2566 nm, where, e.g., trace amounts of acetylene and HF gas can be detected. In the configuration with TM polarization, we demonstrated several advantages of this waveguide: i) Strong light–matter interaction of up to 109% as compared to a free-space beam; ii) reduced requirements for material transparency due to weak light interaction with the waveguide core material, nominally 14% for T = 400 nm and 9% for T = 350 nm; and iii) low coupling loss in an end-fire configuration down to 2.3 dB per facet without any tapers. Nevertheless, minimum experimental propagation losses are still rather high, 6.8 dB cm^{-1}, which likely comes from water and OH absorption in the tantala material. The material transparency needs to be improved to allow longer pathlengths and thus better interaction for sensitivity-critical applications such as trace gas spectroscopy. Future work will thus focus on reducing the material absorption and new cross-sectional designs suppressing the lateral leakage, while making use of the versatile SF_6 plasma etching process.

Funding. Norges Forskningsråd (221860/F60, 262608, 295864); Tromsø Forskningsstiftelse (17_SG_JJ); European Research Council (758973); Engineering and Physical Sciences Research Council (EP/N00762X/1).

Acknowledgments. The authors thank to Jens Høvik, Jong Wook Noh, and Mukesh Yadav (NTNU, Trondheim, Norway) for help with processing, Vinita Mittal (ORC, Southampton, UK) for conducting the XeF_2 etching and Jan Torgersen (NTNU, Trondheim, Norway) for helpful discussions within material processing.

Disclosures. The authors declare no conflicts of interest.

Data availability. Data underlying the results presented in this paper are available in Data File 1, Data File 2, Data File 3 and Data File 4.

References

1. R. Soref, "Mid-infrared photonics in silicon and germanium," Nat. Photonics **4**(8), 495–497 (2010).
2. T. Schädle and B. Mizaikoff, "Mid-infrared waveguides: a perspective," Appl. Spectrosc. **70**(10), 1625–1638 (2016).
3. H. Lin, Z. Luo, T. Gu, L. C. Kimerling, K. Wada, A. Agarwal, and J. Hu, "Mid-infrared integrated photonics on silicon: a perspective," Nanophotonics **7**(2), 393–420 (2017).
4. D. Marris-Morini, V. Vakarin, J. M. Ramirez, Q. Liu, A. Ballabio, J. Frigerio, M. Montesinos, C. Alonso-Ramos, X. Le Roux, S. Serna, D. Benedikovic, D. Chrastina, L. Vivien, and G. Isella, "Germanium-based integrated photonics from near- to mid-infrared applications," Nanophotonics **7**(11), 1781–1793 (2018).
5. H. D. Downing and D. Williams, "Optical constants of water in the infrared," J. Geophys. Res. **80**(12), 1656–1661 (1975).
6. E. Franke, C. L. Trimble, M. J. DeVries, J. A. Woollam, M. Schubert, and F. Frost, "Dielectric function of amorphous tantalum oxide from the far infrared to the deep ultraviolet spectral region measured by spectroscopic ellipsometry," J. Appl. Phys. **88**(9), 5166–5174 (2000).
7. T. J. Bright, J. I. Watjen, Z. M. Zhang, C. Muratore, A. A. Voevodin, D. I. Koukis, D. B. Tanner, and D. J. Arenas, "Infrared optical properties of amorphous and nanocrystalline Ta_2O_5 thin films," J. Appl. Phys. **114**(8), 083515 (2013).
8. Z. Yongheng and G. Zhenan, "The study of removing hydroxyl from silica glass," J. Non-Cryst. Solids **352**(38-39), 4030–4033 (2006).
9. G. Beshkov, S. Lei, V. Lazarova, N. Nedev, and S. S. Georgiev, "IR and Raman absorption spectroscopic studies of APCVD, LPCVD and PECVD thin SiN films," Vacuum **69**(1-3), 301–305 (2002).
10. S. C. Mao, S. H. Tao, Y. L. Xu, X. W. Sun, M. B. Yu, G. Q. Lo, and D. L. Kwong, "Low propagation loss SiN optical waveguide prepared by optimal low-hydrogen module," Opt. Express **16**(25), 20809 (2008).

Optical Materials EXPRESS

11. X. Wu, J. Feng, X. Liu, and H. Zeng, "Effects of rapid thermal annealing on aluminum nitride waveguides," Opt. Mater. Express **10**(12), 3073 (2020).
12. S. A. Miller, M. Yu, X. Ji, A. G. Griffith, J. Cardenas, A. L. Gaeta, and M. Lipson, "Low-loss silicon platform for broadband mid-infrared photonics," Optica **4**(7), 707 (2017).
13. Z. Cheng, X. Chen, C. Y. Wong, K. Xu, and H. K. Tsang, "Mid-infrared suspended membrane waveguide and ring resonator on silicon-on-insulator," IEEE Photonics J. **4**(5), 1510–1519 (2012).
14. J. S. Penades, A. Ortega-Moñux, M. Nedeljkovic, J. G. Wangüemert-Pérez, R. Halir, A. Z. Khokhar, C. Alonso-Ramos, Z. Qu, I. Molina-Fernández, P. Cheben, and G. Z. Mashanovich, "Suspended silicon mid-infrared waveguide devices with subwavelength grating metamaterial cladding," Opt. Express **24**(20), 22908 (2016).
15. J. S. Penadés, A. Sánchez-Postigo, M. Nedeljkovic, A. Ortega-Moñux, J. G. Wangüemert-Pérez, Y. Xu, R. Halir, Z. Qu, A. Z. Khokhar, A. Osman, W. Cao, C. G. Littlejohns, P. Cheben, I. Molina-Fernández, and G. Z. Mashanovich, "Suspended silicon waveguides for long-wave infrared wavelengths," Opt. Lett. **43**(4), 795–798 (2018).
16. W. Zhou, Z. Cheng, X. Wu, X. Sun, and H. K. Tsang, "Fully suspended slot waveguide platform," J. Appl. Phys. **123**(6), 063103 (2018).
17. T.-H. Xiao, Z. Zhao, W. Zhou, C.-Y. Chang, S. Y. Set, M. Takenaka, H. K. Tsang, Z. Cheng, and K. Goda, "Mid-infrared high-Q germanium microring resonator," Opt. Lett. **43**(12), 2885 (2018).
18. A. Osman, M. Nedeljkovic, J. Soler Penades, Y. Wu, Z. Qu, A. Z. Khokhar, K. Debnath, and G. Z. Mashanovich, "Suspended low-loss germanium waveguides for the longwave infrared," Opt. Lett. **43**(24), 5997 (2018).
19. A. Abdou, P. Panduranga, J. Richter, E. L. H. Thomas, S. Mandal, O. A. Williams, J. Witzens, and M. P. Nezhad, "Air-clad suspended nanocrystalline diamond ridge waveguides," Opt. Express **26**(11), 13883–13890 (2018).
20. T. J. Kippenberg, J. Kalkman, A. Polman, and K. J. Vahala, "Demonstration of an erbium-doped microdisk laser on a silicon chip," Phys. Rev. A **74**(5), 051802 (2006).
21. S. Sridaran and S. A. Bhave, "Nanophotonic devices on thin buried oxide silicon-on-insulator substrates," Opt. Express **18**(4), 3850 (2010).
22. N. Nader, A. Kowligy, J. Chiles, E. J. Stanton, H. Timmers, A. J. Lind, F. C. Cruz, D. M. B. Lesko, K. A. Briggman, S. W. Nam, S. A. Diddams, and R. P. Mirin, "Infrared frequency comb generation and spectroscopy with suspended silicon nanophotonic waveguides," Optica **6**(10), 1269 (2019).
23. J.-C. Tinguely, Ø. I. Helle, and B. S. Ahluwalia, "Silicon nitride waveguide platform for fluorescence microscopy of living cells," Opt. Express **25**(22), 27678–27690 (2017).
24. Ø. I. Helle, F. T. Dullo, M. Lahrberg, J.-C. Tinguely, O. G. Hellesø, and B. S. Ahluwalia, "Structured illumination microscopy using a photonic chip," Nat. Photonics **14**(7), 431–438 (2020).
25. P. M. Sarro, A. W. van Herwaarden, and W. van der Vlist, "A silicon-silicon nitride membrane fabrication process for smart thermal sensors," Sens. Actuators, A **42**(1-3), 666–671 (1994).
26. S. Lorenzo and O. Solgaard, "Optical fiber-facet multiplexed monolithic silicon pressure sensors," IEEE Sens. J. **20**(18), 10598–10606 (2020).
27. M. Ghaderi and R. F. Wolffenbuttel, "Design and fabrication of ultrathin silicon-nitride membranes for use in UV-visible airgap-based MEMS optical filters," J. Phys.: Conf. Ser. **757**, 012032 (2016).
28. T. S. English, J. Provine, A. F. Marshall, A. L. Koh, and T. W. Kenny, "Parallel preparation of plan-view transmission electron microscopy specimens by vapor-phase etching with integrated etch stops," Ultramicroscopy **166**, 39–47 (2016).
29. X. Liu, M. M. Skanata, and D. Stein, "Entropic cages for trapping DNA near a nanopore," Nat. Commun. **6**(1), 6222 (2015).
30. G. Li, T. Maruyama, and K. Iiyama, "Low-propagation-loss Ta_2O_5 optical waveguides on silica substrate," Jpn. J. Appl. Phys. **53**(4S), 04EG12 (2014).
31. A. Z. Subramanian, G. S. Murugan, M. N. Zervas, and J. S. Wilkinson, "Spectroscopy, modeling, and performance of erbium-doped Ta_2O_5 waveguide amplifiers," J. Lightwave Technol. **30**(10), 1455–1462 (2012).
32. D. Saygin-Hinczewski, K. Koc, I. Sorar, M. Hinczewski, F. Z. Tepehan, and G. G. Tepehan, "Optical and structural properties of Ta_2O_5–CeO_2 thin films," Sol. Energy Mater. Sol. Cells **91**(18), 1726–1732 (2007).
33. M. Vlk, A. Datta, S. Alberti, H. D. Yallew, V. Mittal, G. S. Murugan, and J. Jágerská, "Extraordinary evanescent field confinement waveguide sensor for mid-infrared trace gas spectroscopy," Light Sci. Appl. **10**(1), 26 (2021).
34. T. D. Visser, H. Blok, B. Demeulenaere, and D. Lenstra, "Confinement factors and gain in optical amplifiers," IEEE J. Quantum Electron. **33**(10), 1763–1766 (1997).
35. J. T. Robinson, K. Preston, O. Painter, and M. Lipson, "First-principle derivation of gain in high-index-contrast waveguides," Opt. Express **16**(21), 16659–16669 (2008).
36. F. Ottonello-Briano, C. Errando-Herranz, H. Rödjegård, H. Martin, H. Sohlström, and K. B. Gylfason, "Carbon dioxide absorption spectroscopy with a mid-infrared silicon photonic waveguide," Opt. Lett. **45**(1), 109 (2020).
37. G. J. Veldhuis, O. Parriaux, H. J. W. M. Hoekstra, and P. V. Lambeck, "Sensitivity enhancement in evanescent optical waveguide sensors," J. Lightwave Technol. **18**(5), 677–682 (2000).
38. M. A. Webster, R. M. Pafchek, A. Mitchell, and T. L. Koch, "Width dependence of inherent TM-mode lateral leakage loss in silicon-on-insulator ridge waveguides," IEEE Photonics Technol. Lett. **19**(6), 429–431 (2007).
39. F. Tsige Dullo, J.-C. Tinguely, S. Andre Solbo, and O. G. Helleso, "Single-mode limit and bending losses for shallow rib Si_3N_4 waveguides," IEEE Photonics J. **7**(1), 1–11 (2015).

Optical Materials EXPRESS

40. C. Chaneliere, J. L. Autran, R. A. B. Devine, and B. Balland, "Tantalum pentoxide (Ta_2O_5) thin films for advanced dielectric applications," Mater. Sci. Eng. R Rep. **22**(6), 269–322 (1998).
41. W. M. Paulson, F. S. Hickernell, and R. L. Davis, "Effects of deposition parameters on optical loss for rf-sputtered Ta_2O_5 and Si_3N_4 waveguides," J. Vac. Sci. Technol. **16**(2), 307–310 (1979).
42. M. F. A. Muttalib, R. Y. Chen, S. J. Pearce, and M. D. B. Charlton, "Anisotropic Ta_2O_5 waveguide etching using inductively coupled plasma etching," J. Vac. Sci. Technol., A **32**(4), 041304 (2014).
43. C. Christensen, R. de Reus, and S. Bouwstra, "Tantalum oxide thin films as protective coatings for sensors," J. Micromech. Microeng. **9**(2), 113–118 (1999).
44. D. Briand, G. Mondin, S. Jenny, P. D. van der Wal, S. Jeanneret, N. F. de Rooij, O. Banakh, and H. Keppner, "Metallo-organic low-pressure chemical vapor deposition of Ta_2O_5 using $TaC_{12}H_{30}O_5N$ as precursor for batch fabrication of microsystems," Thin Solid Films **493**(1-2), 6–12 (2005).
45. M. F. A. Muttalib, R. Y. Chen, S. J. Pearce, and M. D. B. Charlton, "Optimization of reactive-ion etching (RIE) parameters for fabrication of tantalum pentoxide (Ta_2O_5) waveguide using Taguchi method," EPJ Web Conf. **162**, 01003 (2017).
46. K. Sugano and O. Tabata, "Reduction of surface roughness and aperture size effect for etching of Si with XeF_2," J. Micromech. Microeng. **12**(6), 911–916 (2002).
47. C. Frederico, R. Hibert, P. Fritschi, P. Fluckiger, A. M. Renaud, and Ionescu, "Silicon sacrificial layer dry etching (SSLDE) for free-standing RF MEMS architectures," in *The Sixteenth Annual International Conference on Micro Electro Mechanical Systems, 2003. MEMS-03 Kyoto. IEEE* (IEEE, 2003), pp. 570–573.
48. K. P. Larsen, D. H. Petersen, and O. Hansen, "Study of the roughness in a photoresist masked, isotropic, SF_6-based ICP silicon etch," J. Electrochem. Soc. **153**(12), G1051 (2006).
49. T. Zhu, P. Argyrakis, E. Mastropaolo, K. K. Lee, and R. Cheung, "Dry etch release processes for micromachining applications," J. Vac. Sci. Technol., B: Microelectron. Nanometer Struct.–Process., Meas., Phenom. **25**(6), 2553 (2007).
50. P. Panduranga, A. Abdou, Z. Ren, R. H. Pedersen, and M. P. Nezhad, "Isotropic silicon etch characteristics in a purely inductively coupled SF_6 plasma," J. Vac. Sci. Technol., B: Nanotechnol. Microelectron.: Mater., Process., Meas., Phenom. **37**(6), 061206 (2019).
51. H. F. Winters and J. W. Coburn, "The etching of silicon with XeF_2 vapor," Appl. Phys. Lett. **34**(1), 70–73 (1979).
52. D. Xu, B. Xiong, G. Wu, Y. Wang, X. Sun, and Y. Wang, "Isotropic silicon etching With XeF_2 gas for wafer-level micromachining applications," J. Microelectromech. Syst. **21**(6), 1436–1444 (2012).
53. D. E. Ibbotson, D. L. Flamm, J. A. Mucha, and V. M. Donnelly, "Comparison of XeF_2 and F-atom reactions with Si and SiO_2," Appl. Phys. Lett. **44**(12), 1129–1131 (1984).
54. M. Winterkorn, A. L. Dadlani, Y. Kim, J. Provine, and F. B. Prinz, "ETCH 'sandbox': Controlled release dimensions through atomic layer deposition etch stop with trench refill and polish," in *18th International Conference on Solid-State Sensors, Actuators and Microsystems (TRANSDUCERS)* (IEEE, 2015), pp. 2272–2275.
55. R. d'Agostino and D. L. Flamm, "Plasma etching of Si and SiO_2 in SF_6–O_2 mixtures," J. Appl. Phys. **52**(1), 162–167 (1981).
56. D. E. Ibbotson, J. A. Mucha, D. L. Flamm, and J. M. Cook, "Plasmaless dry etching of silicon with fluorine-containing compounds," J. Appl. Phys. **56**(10), 2939–2942 (1984).
57. P. B. Chu, J. T. Chen, R. Yeh, G. Lin, J. C. P. Huang, B. A. Warneke, and S. J. Pister, "Controlled pulse-etching with xenon difluoride," in *Proceedings of International Solid State Sensors and Actuators Conference (Transducers '97)* (IEEE, 1997), Vol. 1, pp. 665–668.
58. K. R. Williams, K. Gupta, and M. Wasilik, "Etch rates for micromachining processing-Part II," J. Microelectromech. Syst. **12**(6), 761–778 (2003).
59. J.-F. Veyan, M. D. Halls, S. Rangan, D. Aureau, X.-M. Yan, and Y. J. Chabal, "XeF_2-induced removal of SiO_2 near Si surfaces at 300 K: an unexpected proximity effect," J. Appl. Phys. **108**(11), 114914 (2010).
60. S. Leopold, C. Kremin, A. Ulbrich, S. Krischok, and M. Hoffmann, "Formation of silicon grass: Nanomasking by carbon clusters in cyclic deep reactive ion etching," J. Vac. Sci. Technol., B: Nanotechnol. Microelectron.: Mater., Process., Meas., Phenom. **29**(1), 011002 (2011).
61. R. A. Gottscho, "Microscopic uniformity in plasma etching," J. Vac. Sci. Technol., B: Microelectron. Process. Phenom. **10**(5), 2133 (1992).
62. R. Smith, M. Tagg, and J. Walls, "Deterministic models of ion erosion, reflection and redeposition," Vacuum **34**(1-2), 175–180 (1984).
63. K. P. Müller and J. Pelka, "Redeposition in ion milling," Microelectron. Eng. **7**(1), 91–101 (1987).